

## PAPER

[View Article Online](#)  
[View Journal](#) | [View Issue](#)Cite this: *J. Mater. Chem. A*, 2017, 5, 9032

## High-performance, ultra-flexible and transparent embedded metallic mesh electrodes by selective electrodeposition for all-solid-state supercapacitor applications†

Yan-Hua Liu,<sup>a</sup> Jian-Long Xu,<sup>id</sup>\*<sup>b</sup> Su Shen,<sup>\*a</sup> Xin-Lei Cai,<sup>b</sup> Lin-Sen Chen<sup>a</sup> and Sui-Dong Wang<sup>\*b</sup>

A novel approach to fabricate large-scale embedded metallic mesh transparent conductive electrodes (TCEs) on flexible substrates via a low-cost and facile selective electrodeposition process combined with inverted film-processing methods is proposed for the first time. The optimized embedded Ni mesh TCEs on polyethylene terephthalate (PET) exhibit excellent optoelectronic properties ( $R_s \sim 0.2 \Omega \text{ sq}^{-1}$  &  $T \sim 84\%$ ), high figure of merit ( $\text{FOM} \sim 1.0 \times 10^4$ ) and mechanical durability properties, which arise from the embedded inverted T-type shape of the electrodeposited Ni mesh. The resultant embedded Ni mesh/polymer poly(3,4-ethylenedioxythiophene):poly(styrenesulfonate) (PEDOT:PSS) hybrid electrodes are utilized both as current collectors and active electrode materials for all-solid-state flexible transparent supercapacitors, which show high transparency, superior electrochemical performances, excellent mechanical flexibility and high capacitance retention. Even after 1000 cycles of repetitive bending with a radius of 2 mm, the capacitance exhibited a decrease within only 5.2%. The high performance can be attributed to the excellent optoelectronic properties of embedded Ni mesh electrodes in combination with superior electrochemical properties of PEDOT:PSS. This provides a simple, cheap and controllable method for fabricating high-performance flexible TCEs and thus constructing flexible and transparent energy conversion and storage devices and systems.

Received 3rd March 2017  
Accepted 30th March 2017

DOI: 10.1039/c7ta01947e

[rsc.li/materials-a](http://rsc.li/materials-a)

## Introduction

Transparent and flexible energy conversion and storage devices are essential components of future wearable electronic systems and have attracted much attention from both academia and industry areas.<sup>1–4</sup> Particularly, transparent and flexible supercapacitors, which can be attached to objects of any shape or biological tissues combined with rapid charge/discharge, high power density and long cycling life, afford an ideal option for integrated power source applications.<sup>5–8</sup> In general, the supercapacitor electrodes should function both as current collectors to transport electrons, and as active materials to store

electrochemical energy.<sup>9</sup> Accordingly, in order to achieve high-performance, flexible and transparent supercapacitors, the most fundamental component of transparent and flexible supercapacitors, electrodes, must exhibit high transparency, conductivity and flexibility, and simultaneously possess excellent electrochemical performances. However, it is still challenging to develop such electrodes based on the existing materials and methods. Recently, there have been increasing efforts in developing novel transparent conductive electrodes (TCEs) including metal nanostructures (metal nanowires and metal grids),<sup>10–12</sup> conductive polymers (PEDOT:PSS)<sup>13,14</sup> and carbon materials (graphene and carbon nanotubes)<sup>15–17</sup> to replace indium tin oxide (ITO) as promising TCEs in future. Nevertheless, their inherent limitations such as low conductivity (carbon materials,  $R_s \sim 30\text{--}1000 \Omega \text{ sq}^{-1}$ ), weak capacitive behaviors (metal nanostructures), moderate optoelectronic behaviors (conductive polymers,  $R_s \sim 100\text{--}450 \Omega \text{ sq}^{-1}$ ) etc. hindered their further applications in high-performance supercapacitors.<sup>10–18</sup> Generally, the electrode materials with excellent optoelectronic properties usually lack superior electrochemical energy behaviors and *vice versa*, which is disadvantageous for flexible and transparent supercapacitors. In order to enable excellent optoelectronic properties while

<sup>a</sup>College of Physics, Optoelectronics and Energy, Key Lab of Advanced Optical Manufacturing Technologies of Jiangsu Province, Key Lab of Modern Optical Technologies of Education Ministry of China, Soochow University, Suzhou, Jiangsu 215006, PR China. E-mail: shen.su@gmail.com

<sup>b</sup>Institute of Functional Nano & Soft Materials (FUNSOM), Jiangsu Key Laboratory for Carbon-Based Functional Materials & Devices, Soochow University, Suzhou, Jiangsu 215123, PR China. E-mail: xujianlong@suda.edu.cn; wangsd@suda.edu.cn

† Electronic supplementary information (ESI) available: SEM images of our obtained embedded metallic mesh TCEs with other patterns, the fabrication process of embedded Ni mesh TCEs on polyimide and supercapacitor performances including CV curves at small scan rates and area capacitance versus scan rate curves. See DOI: 10.1039/c7ta01947e

maintaining superior electrochemical energy behaviors of the TCEs, the most promising strategy is to combine a highly flexible, transparent and conductive material with a pseudocapacitive material, forming hybrid electrode films with optimized performances.<sup>19–21</sup> In such hybrid electrodes, the merits of pseudocapacitive materials and electrode materials are combined to make them suitable for flexible and transparent supercapacitors. For example, Lin *et al.* reported a polyaniline (PANI) electrodeposited multiwalled carbon nanotube-based supercapacitor with improved electrochemical properties and high transmittance ( $\sim 70\%$ ), where PANI and multiwalled carbon nanotubes contribute to electrochemical and conductive properties, respectively.<sup>22</sup>

In recent years, metal TCE-based hybrid electrodes such as metallic fabrics/graphene,<sup>23</sup> metal nanowires/graphene,<sup>24</sup> metal grids/PEDOT:PSS,<sup>20</sup> and metal NWs/polymer<sup>25</sup> *etc.* have been demonstrated as promising and more preferred future supercapacitor electrodes due to their high conductivity, transparency, thermal and air-stability, reproducibility, good flexibility and low costs. Moreover, in contrast with metallic NWs-based TCEs, patterned metallic grids can perfectly eliminate the percolation between NWs, NW–NW junction resistances at grid junctions and random dense distribution of NWs, which benefit from the controllable design and patterning of metal grids. However, the reported patterning methods for metallic grids are usually complicated and time consuming, which often involve metal etching, stamp manufacturing, vacuum thermal evaporation and lift-off processes.<sup>26–28</sup> In addition, the flexible metal grid TCEs are nonplanar with a rise of  $\sim \mu\text{m}$  where the metal is usually directly deposited onto the surfaces of underlying plastic foils. The non-planarity of metal grid TCEs with such a large rise usually leads to poor flexibility properties of metal grid TCEs, while it may also yield electrical short-circuit problems.<sup>29</sup> Moreover, the poor adhesion of the metal to the substrate surface results in delamination between them, making the existing embossed metal grids unsuitable for achieving highly flexible electronic devices.<sup>30,31</sup> Therefore, the development of a simple and low-cost scalable method to fabricate metal-based TCEs with excellent optoelectronic and mechanical properties is desired.

Herein, in this work, we introduce a novel method to achieve artificially designed embedded metallic mesh TCEs on an engineered substrate with controllable optoelectronic and mechanical properties *via* a low-cost and facile electrodeposition process combined with an inverted film-processing method. In our proposed methods, nickel metal (Ni) fills into the patterned micro trenches by a simple electrodeposition process, and then free-standing metallic meshes were obtained after photoresist removal. Then, the coplanar and ultra-flexible embedded metallic mesh TCEs were developed by inverted film-processing methods. An extraordinary optoelectronic performance enhancement can be attained through controlling the geometric construction design and deposition processing conditions. A high-performance supercapacitor with excellent flexibility, transparency and electrochemical behaviors utilizing hybrid TCEs consisting of our developed embedded metallic mesh and PEDOT:PSS was obtained. In such hybrid electrodes,

Ni mesh and PEDOT:PSS compensated the disadvantages of each other and fully combined their merits: firstly, the embedded Ni mesh TCEs greatly reduced the sheet resistance of PEDOT:PSS films and thus offer much more conductive paths for current collection; then, PEDOT:PSS, which is a typical flexible and transparent pseudocapacitive material, could largely improve the electrochemical energy storage behaviors of the embedded Ni mesh; thirdly, they both contribute to the excellent optical transparency of the hybrid electrodes and supercapacitor devices; lastly, the spin-coated PEDOT:PSS layer could enhance the anti-oxidation and anti-corrosion capability of Ni mesh TCEs at positive potentials in electrolytes. This paves a simple, cheap and controllable method of fabricating high-performance TCEs and TCE-based hybrid electrode films for future energy conversion and storage device and systems, and extends the current state-of-the-art performance for transparent flexible supercapacitors.

## Experimental

### Fabrication of the embedded metallic mesh TCEs

The fabrication process of the embedded Ni metallic mesh TCEs on the transparent substrate is given below: first, a photoresist (RZJ-390 PG, Ruihong Electronic Chemical Co., LTD) layer was spin-coated onto a pre-cleaned Ni conductive substrate and the designed TCE micro trench patterns were patterned by laser direct-writing techniques. Then, the Ni metal was selectively electrodeposited inside to fill the defined micro trenches to form uniform Ni metallic mesh structures on the Ni substrate. After photoresist removal, the dispersed UV-curable resin (D10, PhiChem) was drop cast onto the Ni substrate, followed by fixing a flexible poly(ethylene terephthalate) (PET) ( $\sim 20 \mu\text{m}$  thick) layer onto the UV resin through a roll-to-roll process. Then, the UV resin was cured by exposure to UV light ( $1000 \text{ mW cm}^{-2}$ , LED LAMPLIC) for only 2 s. Following the curing step, the PET structure was peeled off from the Ni substrate and the flexible and transparent embedded Ni mesh TCE can be obtained.

### Fabrication of embedded Ni mesh/PEDOT:PSS hybrid TCEs

**Embedded Ni mesh/PEDOT:PSS hybrid TCEs were obtained by spin-coating PEDOT:PSS solution onto the as-fabricated embedded Ni mesh TCEs.** The spin-coated PEDOT:PSS solution was prepared by mixing PEDOT:PSS solution with 7 wt% ethylene glycol (EG) and 0.25 wt% surfactant (Triton-X 100). Before spin-coating, the embedded Ni mesh on PET was treated with oxygen plasma for 10 s. The prepared PEDOT:PSS solution was spin-coated onto the embedded Ni mesh surfaces at 3000 rpm for 60 s and then annealed at  $120^\circ\text{C}$  for 20 min in air ambient. The thickness of the PEDOT:PSS film on the embedded Ni mesh electrodes is about 80 nm.

### Preparation of the all-solid-state supercapacitors

The polymer electrolyte (PE) was prepared by mixing poly(vinyl alcohol) (PVA) powder (Aladdin, 10 g), phosphoric acid ( $\text{H}_3\text{PO}_4$ ) (10 mL) and deionized water (90 mL) and then heating and

magnetically stirring at 90 °C for 2 hours. The PVA : H<sub>3</sub>PO<sub>4</sub> ratio in the PE was fixed at 1 : 1 w/v. After being fully mixed, the homogeneous solution is sequentially drop-dispersed on the embedded Ni mesh/PEDOT:PSS hybrid TCEs. Subsequently, with the assembly of another hybrid TCE film, the PE solution was spread over between the two TCE films. The two such PE-coated hybrid electrodes on the PET layer were painted with silver paste and attached to the copper wires to fabricate a symmetrical all-solid-state supercapacitor device by drying in air ambient for 2 days.

### Characterization

Field emission scanning electron microscopy (SEM) (FESEM: JEOL, JSM-5400, USA) was used to characterize the surface morphology and cross-sectional microstructures of the embedded Ni metallic mesh TCEs. The thickness of the PEDOT:PSS film was measured by using a step profiler (XP-200, Ambios Technology, Inc.). The collimated transmittance spectra in the visible range (300–800 nm) and sheet resistance levels of the fabricated samples were measured using a UV-vis spectrophotometer (UV-2550, SHIMADZU) and a four-point probe (CMT SR2000, A. I. T.), respectively. The supercapacitor behaviors were tested in a two-electrode system with a CHI 660B electrochemical workstation (Shanghai CH Instrument Company, China).

## Results and discussion

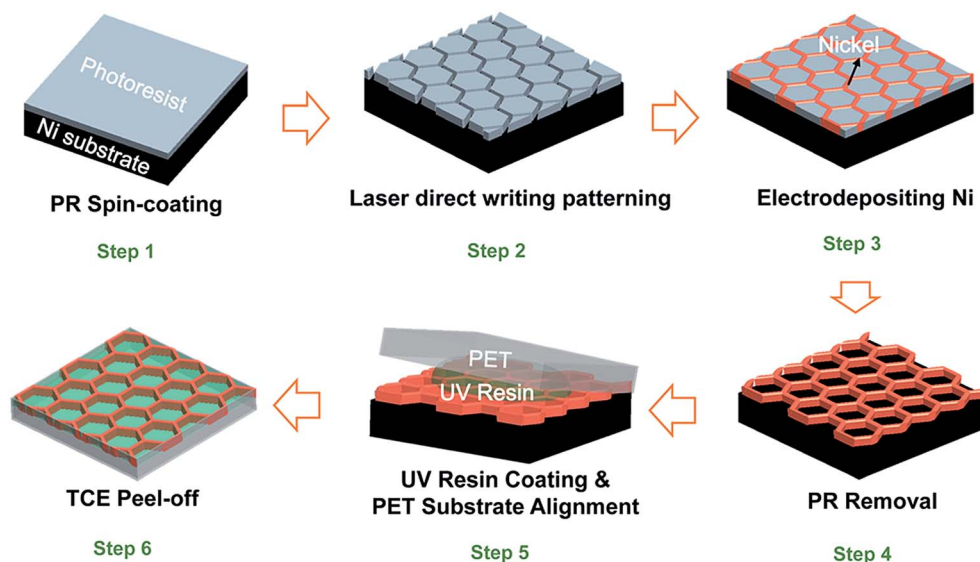
### Fabrication and characterization

The fabrication procedure of the embedded Ni mesh TCEs on the PET layer can be seen in Scheme 1, as described in the Experimental section. Fig. 1 presents the optical images of our fabricated embedded Ni mesh TCEs according to the above-mentioned fabrication procedure. The fabricated TCE exhibits excellent flexibility properties (Fig. 1a(i)) and the TCE

fabrication method can be readily scaled up to realize TCEs with large sizes up to 16 cm × 12 cm, as shown in Fig. 1a(ii). Moreover, the optical and electrical conductivity properties are still excellent when it reaches to a large scale as can be seen in Fig. 1a(iii), demonstrating that our fabricated embedded Ni mesh TCE is promising for realizing large-area electronic systems. Fig. 1b(i) presents the scanning electronic microscopy (SEM) images of our obtained embedded Ni mesh TCE. It can be seen that the metallic Ni networks with hexagonal structural arrangements resulting from the selective electrodeposition process restricted by the defaulted microgrooves defined as needed are uniform and well-shaped over large areas.

A side-view SEM image of a single Ni metal wire in Fig. 1b(ii) indicates that the metallic Ni mesh is firmly attached to the substrates, well embedded into the UV resin, extremely smooth and naturally interconnected at their junctions, exhibiting solid ribbons with inverted T-type cross sections. The electrodeposited Ni mesh forms a highly dense, smooth, uniform, and interconnected network, as shown in Fig. 1b(iii). The improvement achieved here can be ascribed to the spatially uniform network that is a consequence of the regular distributed Ni mesh acquired by the selective electrodeposition process. The obtained inverted T-type shaped solid Ni ribbons embedded well into the UV resin are much beneficial for the excellent ultra-flexibility properties rather than the vertical shaped solid Ni ribbons. In addition, the successive interconnected structure of the coplanar metal wires can avoid the creation of a large junction resistance, breaking the bottlenecks of metal NW networks.

The width of the metallic Ni ribbon is measured to be ~3 μm and can be adjusted by controlling the designed microgroove width and deposition time. The typical thickness of the metal ribbon is ~1.5 μm, and can be modulated by varying the electrodeposition time according to the performance requirements. The TCEs with other metallic mesh arrangements such as rectangle, brick wall, *etc.* are also fabricated as can be seen in



Scheme 1 Schematic illustration of the fabrication procedure of embedded Ni mesh TCEs.



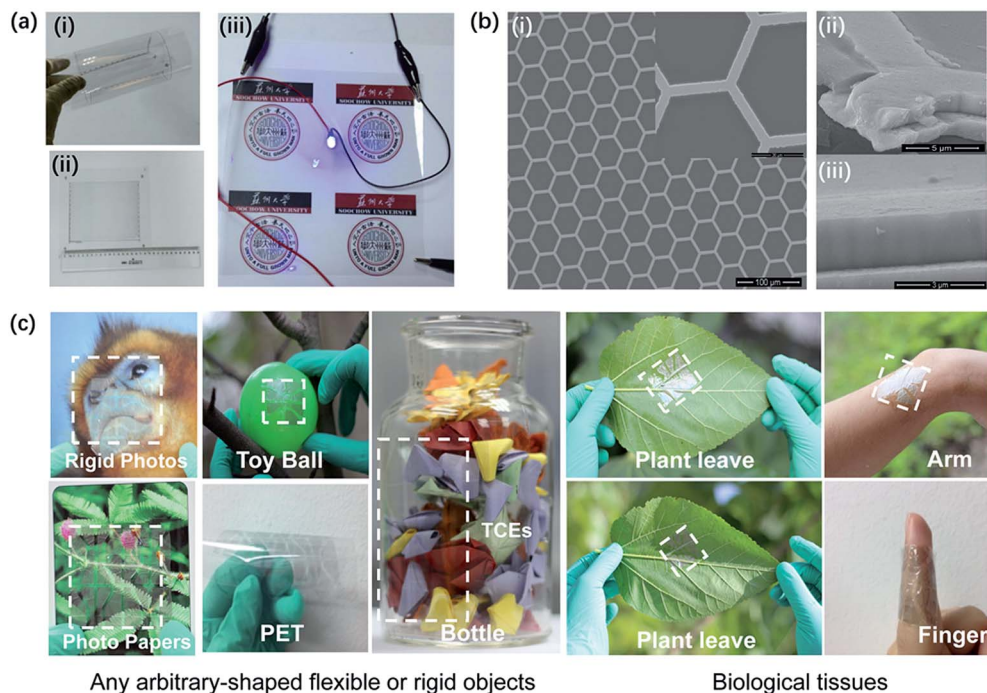


**Fig. 1** Structural characterization of the embedded metallic Ni mesh TCEs: (a) photographs of the fabricated embedded Ni mesh TCE, indicating its (i) excellent flexibility, (ii) the detailed size (16 cm  $\times$  12 cm) of our fabricated embedded Ni mesh TCE on flexible PET and (iii) high optical transparency and electrical conductivity properties. (b) (i) Top-view and (ii) cross-sectional SEM images of the embedded Ni mesh TCE structure, and (iii) presents the enlarged cross-sectional SEM image indicating the high quality of the electrodeposited Ni mesh. (c) The images of Ni mesh TCEs on PI transferred onto any arbitrary-shaped flexible or rigid objects, or biological tissues.

the SEM images (Fig. S1<sup>†</sup>), indicating the excellent universality properties of our fabrication methods of metallic mesh TCEs proposed above. Moreover, polyimide (PI) is also utilized as the polymer matrix and flexible substrate instead of UV resin and PET because it is biocompatible, transparent, flexible, high-temperature tolerant and resistant to chemicals necessary for further process steps when used for practical device applications.<sup>32</sup> The experimental details for the fabrication of embedded Ni mesh TCEs on PI can be seen in Fig. S2.<sup>†</sup> After fabrication, the chip was placed in DI water at RT to relieve stress and release the embedded Ni mesh TCE structure. For a 10 cm  $\times$  10 cm TCE, this operation takes  $\sim$ 20 min after which the TCEs float on the water surface. The TCE can then be fished and transferred onto any arbitrary-shaped rigid or flexible support or any biological tissues or implantable devices, as shown in Fig. 1c, indicating its ultra-flexibility and compatible properties.

### Optoelectronic properties of embedded Ni mesh TCEs

The performances of the embedded Ni mesh TCEs were first characterized by measuring the light transmittance, haze and lateral electrical sheet resistance values. Fig. 2a presents the optical transmission spectra of the hexagonally arranged Ni-mesh TCE with a metal wire width of 4.5  $\mu$ m, network period of 150  $\mu$ m and electrodeposited Ni thickness ranging from 0.8  $\mu$ m to 3.5  $\mu$ m. It can be seen that the resulting embedded Ni mesh TCEs all exhibit a high transmittance of 84–89% with the pure PET exhibiting a 92% transmittance, making it promising for

future transparent electronics. Moreover, the transmittance decreases from 89.4% to 87.52% (at 550 nm) with the increase of electrodeposited Ni thickness from 0.8  $\mu$ m to 3.5  $\mu$ m. On the other hand, the corresponding haze values of the above-fabricated TCEs are all lower than 2% in the visible region, which is comparable to that of commercial ITO TCEs, as presented in Fig. 2b. Sheet resistance is measured by a four-probe method, and the reported resistance value of each sample is the average value of five measurements. The sheet resistance of embedded Ni mesh TCEs with the network period of 150  $\mu$ m decreased from 1.5  $\Omega$  sq<sup>-1</sup> to 0.2  $\Omega$  sq<sup>-1</sup> as the Ni thickness increased from 0.8  $\mu$ m to 3.5  $\mu$ m (Fig. 2c), while very low optical transmittance loss <5% is caused at the same time. Moreover, when the metallic network period reduced to 50  $\mu$ m, the resulted embedded Ni mesh TCE exhibits similar relationships with the Ni thickness that the sheet resistance decreases from 0.9  $\Omega$  sq<sup>-1</sup> to 0.02  $\Omega$  sq<sup>-1</sup> with the Ni thickness ranging from 0.7  $\mu$ m to 4.5  $\mu$ m, which is much smaller than that of the TCE with a network period of 150  $\mu$ m. Thus, it can be inferred that the optical transmittance and electrical conductivity properties of the embedded Ni mesh TCE can be altered by varying the network period and Ni metal thickness as designed. Using the aforementioned electrodeposition technique, the Ni thickness that corresponds to the filling height of the Ni in the micro-groove mesh can be easily controlled and altered by tuning the electrodeposition time without any high vacuum or specialized equipment and any considerable lateral dimension propagation due to its additive manufacturing nature, providing a feasible way to improve the electric conductivity without obvious optical

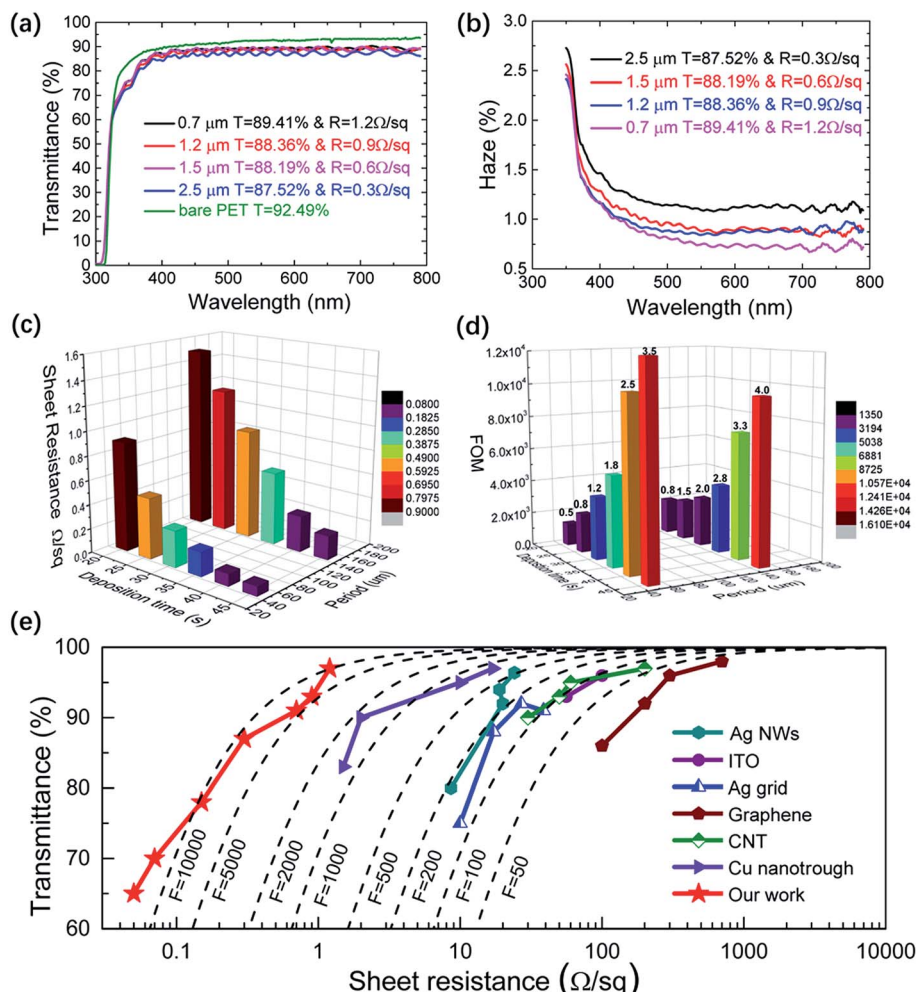


Fig. 2 Optical and electrical characterization of embedded Ni mesh TCEs: (a) optical transmittance spectrum of commercial PET films and the embedded Ni mesh TCEs on PET with the Ni thickness ranging from 0.7  $\mu\text{m}$  to 2.5  $\mu\text{m}$ . (b) Haze spectrum of embedded Ni mesh TCEs with varying Ni thicknesses. A 3D bar graph displaying the (c) sheet resistance and (d) FOM values obtained from the embedded Ni mesh TCEs fabricated under conditions: spacing of 50  $\mu\text{m}$  and 150  $\mu\text{m}$ , and deposition time of 20, 25, 30, 35, 40 or 45 s. (e) The optical transmittance versus the corresponding sheet resistance of embedded Ni mesh TCEs at a wavelength of 550 nm. The performances of commercial ITO films, CNTs,<sup>17</sup> graphene,<sup>37</sup> Ag NWs,<sup>35,36,38,40,41</sup> Ag grids<sup>39</sup> and Cu nanotroughs<sup>34</sup> are also shown for comparison. The solid marks represent the FOM values excluding the substrate contribution. It should be noted that the transmittance mentioned here excludes the substrate effects.

transmittance loss for future high-performance, large-scale and low-cost TCEs and TCE-based electronic circuits and systems.

Fig. 2d shows the figure of merit (FOM) properties of our obtained embedded Ni mesh TCEs with different Ni thicknesses and metal network periods. The FOM proposed by Haacke is defined as follows:  $\text{FOM} = \sigma_{\text{dc}}/\sigma_{\text{opt}} = 188.5/R_s(T^{1/2} - 1)$ , where  $\sigma_{\text{dc}}$  and  $\sigma_{\text{opt}}$  are the electrical and optical conductivity, respectively, and  $R_s$  and  $T$  are the sheet resistance and optical transmittance of TCEs, respectively.<sup>33</sup> The higher value of FOM corresponds to a high value of  $T$  or a low value of  $R_s$ , preferable for high-performance TCEs. The FOM value of embedded Ni-mesh TCEs extracted and calculated from Fig. 2a and c increased from  $1.4 \times 10^3$  to  $1.2 \times 10^4$  (for a metal network period of 50  $\mu\text{m}$ ),  $2.0 \times 10^3$  to  $1.0 \times 10^4$  (for a metal network period of 150  $\mu\text{m}$ ), respectively, with the increase of the electrodeposited Ni thickness, as shown in Fig. 2d. The obtained maximum FOM is calculated to be  $1.2 \times 10^4$ , higher than most

reported TCEs, with the Ni thickness of 4.5  $\mu\text{m}$  and the Ni network period of 50  $\mu\text{m}$ . Noticeably, as the electrodeposited Ni thickness increases,  $R_s$  decreases notably while  $T$  decreases negligibly, thus a large increase of FOM values as high as  $1.2 \times 10^4$  is induced, as obviously demonstrated in Fig. 2d. Moreover, the electro-optical properties of our fabricated embedded Ni mesh TCEs and other reported TCEs are summarized in Fig. 2e, which represents  $R_s$  versus  $T$  at a wavelength of 550 nm. The embedded Ni mesh TCE in this work demonstrates the  $R_s$ - $T$  performances ( $T = 84\%$  (550 nm),  $R_s = 0.2 \Omega \text{ sq}^{-1}$  and  $\text{FOM} = 1.0 \times 10^4$  with a Ni thickness of 3.5  $\mu\text{m}$  and the network period of 150  $\mu\text{m}$ ) superior to other TCEs reported in the literature such as commercial ITO films, carbon nanotubes (CNTs), graphene, solution-processed Ag NWs, Ag grids and Cu nanotroughs.<sup>17,34-41</sup> These promising results imply that the embedded metal mesh TCEs fabricated *via* electrodeposition methods provide us a facile, efficient and cost-effective route to

boost the  $R_s$ - $T$  performances of the metallic mesh TCEs for future flexible and stretchable transparent electronics.

### Mechanical flexibility and durability of the embedded Ni mesh TCEs

To investigate the mechanically flexible and robust properties of embedded Ni mesh TCEs, the electrical conductivity properties before and after bending measurements were characterized. In the measurements, the  $R_s$  values of the TCEs were measured after bending them to different radii or repetitively bending it to a radius of 10 mm for 10 000 times with the ITO/PET TCE as comparison. Fig. 3a shows the change of sheet resistance values with bending tests of different radii. When the bending radius decreases to 0.5 mm, the resistance of ITO films increases by almost two orders of magnitude, whereas the resistance of the embedded Ni mesh TCE showed nearly no increase. Moreover, after repetitive  $10^4$  times bending processes, the resistance of the TCE only changed slightly while the ITO films exhibit a large sheet resistance increase and become nearly nonconductive, as presented in Fig. 3b. On examining the Ni-mesh/PET TCEs after the bending regime, we found no significant damage and degradation of surface morphologies, whereas serious surface cracks and severe degradation are observed in ITO films after bending to 10 mm more than 50 times as shown in the inset of Fig. 3b. The mechanical stability can be further confirmed by repeated 3M Scotch tape tests performed on embedded Ni mesh TCEs, where only a slight fluctuation (within  $0.02 \Omega \text{ sq}^{-1}$ ) in the sheet resistance value was caused during and after 100 3M Scotch tape test cycles (Fig. 3c). It proves the excellent adhesion to the substrate of the Ni metal mesh.

All these figures (Fig. 3a–c) prove the high mechanical stability of embedded Ni mesh TCEs, which is attributed to the embedded nature, especially the inverted T-type shaped solid Ni ribbons firmly embedded into the UV resin (Fig. 3d). In traditional embedded metallic mesh TCEs, as shown in the left part of Fig. 3d, owing to the poor adhesion properties between the metallic mesh and the UV resin, the metallic mesh will be separated from the UV resin after bending and result in some surface damage and metallic interconnects, which will further cause poor surface roughness and possible nonconductivity. However, in our embedded metallic mesh TCEs, the metallic mesh is inverted T-shaped, as shown in the SEM images (Fig. 2b). After bending, the T-type shaped Ni ribbons will not separate from the UV resin (Fig. 3d). The TCE retained stability and high conductivity under bending and unfolding conditions, as also confirmed in Fig. 2e. After bending and unfolding to arbitrary angles or shapes, it remains conductive and thus the LED lamp can be lighted. Therefore, the pronounced bending stability properties of embedded Ni mesh TCEs shown in Fig. 3 qualify them to be a flexible TCE for flexible optoelectronic device applications.

### Electrochemical characterization of flexible and transparent supercapacitors based on embedded Ni mesh/PEDOT:PSS hybrid TCEs

The energy storage device developed in this study is the flexible, transparent and symmetric supercapacitor device composed of

embedded Ni mesh/PEDOT:PSS hybrid TCEs and the poly(vinyl alcohol)–phosphoric acid (PVA- $\text{H}_3\text{PO}_4$ ) gel electrolyte, as shown in Fig. 4a. In the supercapacitor device, the embedded Ni mesh is adopted as the current collector and PEDOT:PSS mainly acts as the active material for energy storage where the PVA- $\text{H}_3\text{PO}_4$  layer sandwiched between two identical hybrid electrodes provides a medium for ionic transport. A digital photograph of the flexible and transparent supercapacitor device is shown in Fig. 4b, indicating its high optical transparency ( $\sim 83\%$ ) that resulted from the excellent optical transparency of both hybrid electrode films and the gel electrolyte.

Fig. 4c presents the typical cyclic voltammetry (CV) curves of a single supercapacitor device at a scan rate of 0.5, 5, 10, 20, 50 and  $100 \text{ V s}^{-1}$ . The supercapacitor device shows nearly rectangular CV curves, even at a scan rate as high as  $100 \text{ V s}^{-1}$ , indicating the good energy capacitive performances and excellent rate capability. Besides, the CV curves of the above-mentioned supercapacitor device at low scan rates of 0.05, 0.1 and  $0.2 \text{ V s}^{-1}$  also indicate excellent capacitive performances (Fig. S3†). The embedded Ni mesh/PEDOT:PSS hybrid electrode corresponds to a much higher current compared with the bare embedded Ni mesh TCE. At a low voltage scan rate of  $0.05 \text{ V s}^{-1}$ , the area capacitance  $C_A$  of the supercapacitor is calculated to be  $0.52 \text{ mF cm}^{-2}$ , decreasing to  $0.49 \text{ mF cm}^{-2}$  with the scan rate increasing to  $1.0 \text{ V s}^{-1}$ , as shown in Fig. S4.† Moreover,  $C_A$  decreases to  $0.42 \text{ mF cm}^{-2}$  and  $0.18 \text{ mF cm}^{-2}$ , respectively, when the scan rate increases to 5 and  $100 \text{ V s}^{-1}$ . The electrochemical properties shown above are even larger than those of most reported electric double-layer capacitors (EDLCs) with active electrode materials including nanoporous carbon, graphene, carbon nanotubes, *etc.*<sup>42–44</sup> Although EDLC supercapacitors with electrodes such as reduced graphene oxide, graphene microribbons, *etc.* present a much higher volumetric capacitance, they exhibit much poorer rate capability and frequency response properties.<sup>45,46</sup> Fig. 4d shows the galvanostatic charge/discharge (GCD) curves of the corresponding supercapacitor device at a current density of  $2.22 \text{ mA cm}^{-2}$ , which is fairly symmetric, approximately triangular and does not exhibit an obvious  $IR$  drop at the onset of the GCD discharging process. Particularly, one single charge/discharge process only requires about 0.2 s, which is much lower than most reported EDLC supercapacitor devices.<sup>19–21,42–46</sup> This is indicative of the fast charge propagation process across electrodes, low equivalent series resistance (ESR) and the high coulombic efficiency. In addition, the coulombic efficiency  $n$  was calculated as follows:  $n = t_d/t_c$  where  $t_d$  and  $t_c$  are the time required for discharging and charging the supercapacitors, respectively. Fig. 4e shows the calculated coulombic efficiency of the supercapacitor device at various current densities. The coulombic efficiency is 96.29% at a current density of  $0.44 \text{ mA cm}^{-2}$  and increases to 100% when the current density reaches  $1.32 \text{ mA cm}^{-2}$ , indicating extra high charge/discharge efficiency of the device. With the applied current density ranging from 0.44 to  $2.22 \text{ mA cm}^{-2}$ , the corresponding GCD curves are presented in Fig. 4f. All GCD curves exhibit good linear profiles, which further confirm the good capacitance behaviour of the device. With the increase of applied current density, the time required for a charge/discharge cycle decreases from 1.1 s ( $0.44$



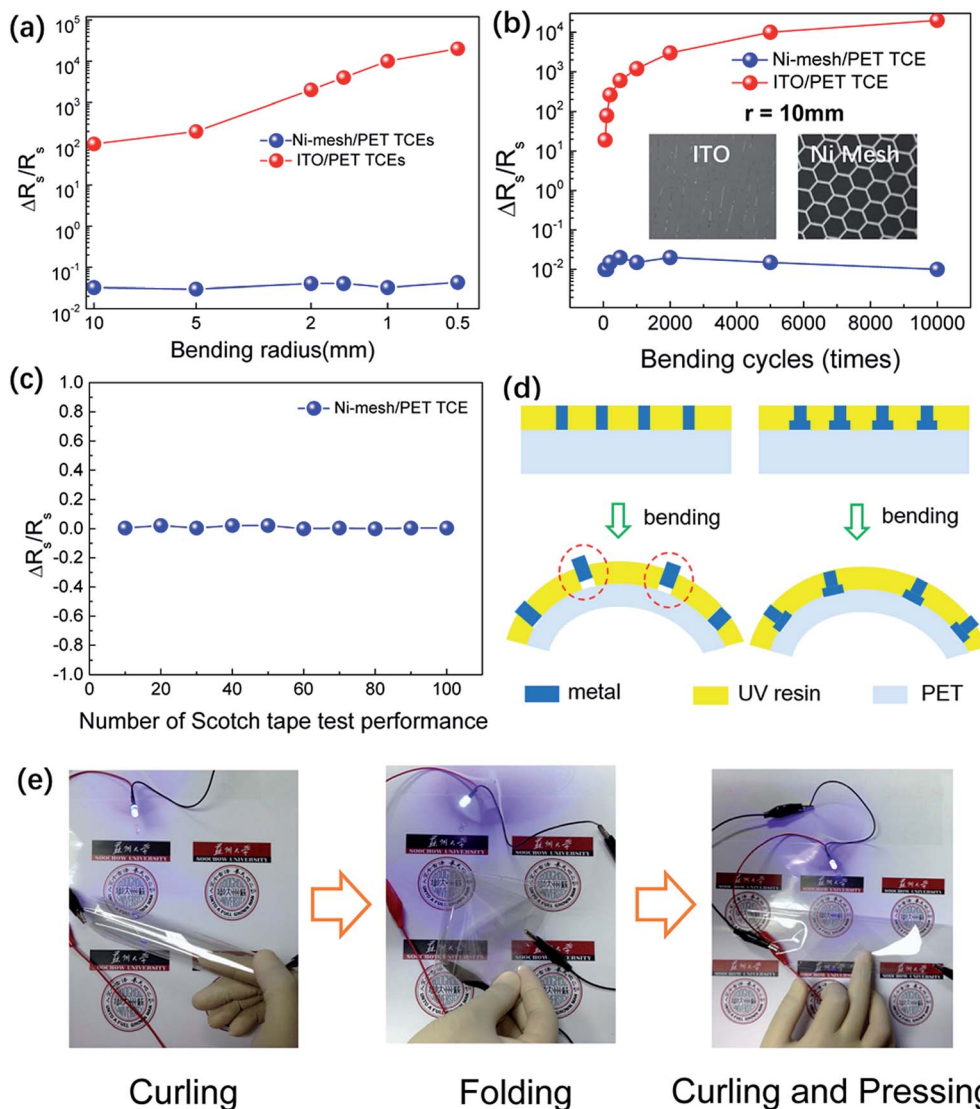


**Fig. 3** Mechanical flexibility and durability properties of embedded Ni mesh TCEs. (a) Sheet resistance change *versus* bending radius properties of embedded Ni mesh TCEs on PET and commercial ITO/PET electrodes. (b) Variations in sheet resistance of an embedded Ni mesh TCE and commercial ITO electrodes on PET substrates as a function of the number of cycles of repetitive bending to a radius of 10 mm. The inset shows the surface morphology of embedded Ni mesh TCEs and ITO films after repetitive bending to a radius of 10 mm for 10 000 times. (c) Sheet resistance change as a function of the number of scotch tape measurements of embedded Ni mesh TCEs. (d) Schematic illustrations of the T-type shaped solid Ni ribbons firmly embedded into the UV resin matrix, indicating the excellent mechanical durability properties of embedded Ni mesh TCEs. (e) Photographs of embedded Ni mesh TCEs. After bending and unfolding, the embedded Ni mesh TCE on PET still remained conductive.

$\text{mA cm}^{-2}$ ) to 0.2 s ( $2.22 \text{ mA cm}^{-2}$ ), indicating faster charge propagation processes across the electrodes than most reported EDLC supercapacitors.

The frequency responses of the devices are also examined by electrochemical impedance spectroscopy (EIS) as presented in Fig. 4g. In the low frequency regions, the straight line was almost parallel to the imaginary axis, which is illustrative of a nearly ideal capacitive behaviour. Meanwhile, in the high frequency regions, the absence of a semicircle-like response observed from the Nyquist plots indicates the high ionic conductivity at the electrode/electrolyte interfaces, consistent with the observed high rate capability performances.<sup>47</sup> The ultra-low (ESR) values estimated from the *x*-intercept in the

Nyquist plots of our supercapacitor device are much lower than those of the most reported EDLC supercapacitors, which could be attributed to the ultra-low resistance value of embedded Ni mesh/PEDOT:PSS hybrid electrodes. Thus, it results in the fast charge propagation processes and consistent with the GCD curves and coulombic efficiencies values shown above. The corresponding Bode plots are shown in Fig. 4h, from which a phase angle of  $\sim 81.5^\circ$  can be seen which is illustrative of excellent electrochemical properties. Moreover, for a more detailed analysis of the EIS results, the normalized imaginary part  $C''$  of the capacitance *versus* frequency curves were calculated and plotted in Fig. 4h. The fast frequency behaviour of the supercapacitor can be illustrated by the short relaxation time

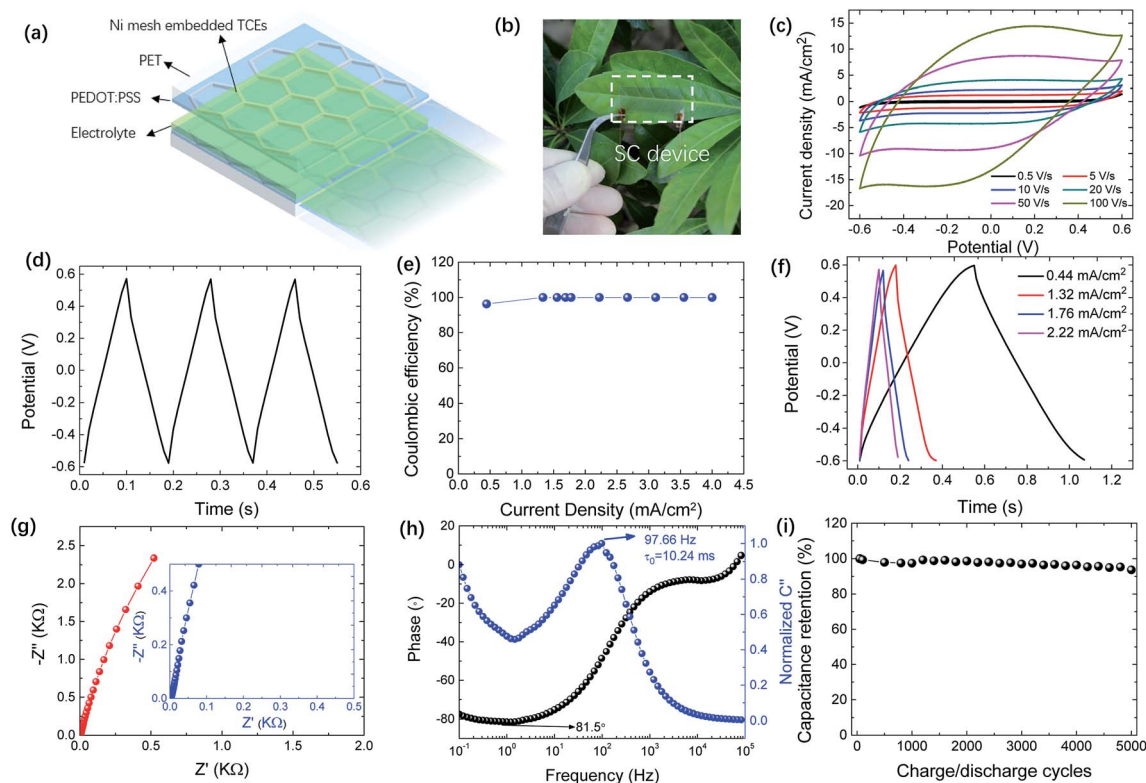


Fig. 4 Electrochemical performances of the flexible and transparent all-solid-state supercapacitors based on embedded Ni mesh/PEDOT:PSS hybrid electrodes: (a) schematic illustrations of a flexible and transparent supercapacitor device based on embedded Ni mesh/PEDOT:PSS hybrid electrodes; (b) digital photographs of a fabricated supercapacitor device; (c) typical CV curves of the supercapacitor device for a scan rate of 0.5, 5, 10, 20, 50 and 100  $\text{V s}^{-1}$ . (d) Potential versus time (GCD plot) for three continuous charge/discharge cycles at an applied current density of 2.22  $\text{mA cm}^{-2}$ . (e) Coulombic efficiency versus current density curves of the supercapacitor device. (f) GCD plots of the supercapacitor device at different applied current densities. (g) Imaginary impedance  $Z''$  versus real impedance  $Z'$  (Nyquist plot) in the frequency range from 0.1 to 100 kHz. The inset shows the magnified part of the low real impedance part; (h) normalized imaginary capacitance  $C''$  versus frequency and phase angle versus frequency curves; (i) capacitance retention versus charge/discharge cycles properties of the supercapacitor device.

constant  $\tau_0$ , determined from the peak frequency of  $C''$  versus  $f$  curves by  $\tau_0 = 1/f_{\text{peak}}$ . It represents the minimum time required for fully discharging the supercapacitor device with an efficiency of  $>50\%$ .<sup>48</sup> The relaxation time constant is extracted and calculated to be 10.24 ms, further confirming the fast charge/discharge processes in Fig. 4d–f. Notably, the above-obtained relaxation time constant of our supercapacitor (10.24 ms) is much smaller than those of conventional active carbon-based supercapacitors (10 s) and comparable with those of reported high-rate supercapacitors (1–30 ms).<sup>44,49,50</sup> Fig. 4i provides insights into the electrochemical stability properties of our flexible and transparent supercapacitor. It can be seen that the device can maintain more than 95% of the initial capacitance value after 5000 continuous charge/discharge cycles, indicating the excellent electrochemical stability of the supercapacitor. Moreover, it also indicates the good encapsulation capacity of the gel electrolyte, which originates from the symmetric sandwiched structure of the supercapacitor and TCEs.

Next, the electrochemical performance stability of the above-mentioned supercapacitor device is measured before and after repeated 1000 bending cycles with a constant bending radius of 2 mm. Our fabricated supercapacitor device exhibits excellent cycling stability in the bending and relaxing tests, indicating its

excellent ultra-flexible properties. As shown in the inset of Fig. 5, after bending for 50, 100, 300, 500 and 1000 cycles with a bending radius of 2 mm, the device shows no noticeable performance degradation in the CV curves with an increase of

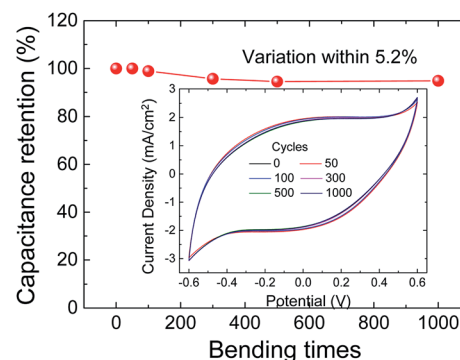


Fig. 5 Capacitance retention versus bending time properties of the transparent and flexible all-solid-state supercapacitors based on embedded Ni mesh/PEDOT:PSS hybrid electrodes with a bending radius of 2 mm. The inset shows CV curves of the supercapacitor device before and after 50, 100, 300, 500 and 1000 bending cycles with a constant bending radius of 2 mm.



bending times. The normalized volumetric capacitance  $C/C_0$  was extracted from the CV curves and plotted in Fig. 5. Even after 1000 cycles of repetitive bending with a radius of 2 mm, it exhibited a decrease within only 5.2%, which indicates that it had highly stable mechanical properties. Thus, as discussed above, the flexible transparent all-solid-state supercapacitors utilizing embedded Ni mesh/PEDOT:PSS hybrid TCEs as current collectors and active electrode materials in this work are promising in future flexible and transparent energy storage fields and enable their further applications as integrated power sources.

## Conclusions

In conclusion, we propose a novel method for fabricating large-scale flexible embedded metallic mesh transparent conductive electrodes (TCEs) on PET substrates by a selective electrodeposition process and inverted film-processing methods. The extraordinary optoelectronic performance improvement can be obtained by controlling the geometric construction design and deposition conditions, where the optimized embedded Ni mesh TCEs exhibit low resistance values of  $0.2\text{--}1.5\ \Omega\ \text{sq}^{-1}$ , high optical transparency of 84–89%, high figure of merit ( $\text{FOM} \sim 1.0 \times 10^4$ ) and superior mechanical flexibility. The excellent mechanical flexibility originates from the embedded inverted T-type shape of the electrodeposited Ni mesh. The flexible and transparent all-solid-state supercapacitors utilizing embedded Ni mesh/PEDOT:PSS hybrid TCEs as both current collectors and active electrode materials are demonstrated with excellent optoelectronic, electrochemical and mechanical durability properties. The embedded Ni mesh and PEDOT:PSS not only compensate their disadvantages but also fully combine their merits, offer much more conductive paths and yield a much lower sheet resistance than both single materials; the PEDOT:PSS layer improves the electrochemical properties of the single embedded Ni mesh which results in good supercapacitor behavior, and also enhances the anti-oxidation and anti-corrosion capability of the Ni mesh at positive potentials in electrolytes. It paves the way for fabricating high-performance and low-cost embedded metallic mesh TCEs and thus constructing hybrid TCE-based flexible and transparent energy storage and conversion systems for future wearable electronics.

## Acknowledgements

We acknowledge financial support from the Natural Science Foundation of China (No. 61405133, 91323303, 61575133, 61675143 and 11661131002), the Natural Science Foundation of Jiangsu Province (No. BK20140348 and BK20160328) and the Specialized Research Fund for the Doctoral Program of Higher Education (No. 20133201120027). This project is also funded by the Collaborative Innovation Center of Suzhou Nano Science and Technology, and by the Priority Academic Program Development of Jiangsu Higher Education Institutions (PAPD).

## Notes and references

- 1 N. Yabuuchi, K. Kubota, M. Dahbi and S. Komaba, *Chem. Rev.*, 2014, **114**, 11636.
- 2 X. F. Wang, Y. Chen, O. G. Schmidt and C. L. Yan, *Chem. Soc. Rev.*, 2016, **45**, 1308.
- 3 X. F. Wang, X. H. Lu, B. Liu, D. Chen, Y. X. Tong and G. Z. Shen, *Adv. Mater.*, 2014, **26**, 4763.
- 4 L. Li, Z. Wu, S. Yuan and X. B. Zhang, *Energy Environ. Sci.*, 2014, **7**, 2101.
- 5 L. B. Dong, C. J. Xu, Y. Li, Z. H. Huang, F. Y. Kang, Q. H. Yang and X. Zhao, *J. Mater. Chem. A*, 2016, **4**, 4659.
- 6 X. B. Zang, Q. Chen, P. X. Li, Y. J. He, X. Li, M. Zhu, X. M. Li, K. L. Wang, M. L. Zhong, D. H. Wu and H. W. Zhu, *Small*, 2014, **10**, 2583.
- 7 H. Lee, S. Hong, J. Lee, Y. D. Suh, J. Kwon, H. Moon, H. Kim, J. Yeo and S. H. Ko, *ACS Appl. Mater. Interfaces*, 2016, **8**, 15449.
- 8 C. M. Chang, Z. H. Hu, T. Y. Lee, Y. A. Huang, W. F. Ji, W. R. Liu, J. M. Yeh and Y. Wei, *J. Mater. Chem. A*, 2016, **4**, 9133.
- 9 Y. G. Wang, Y. F. Song and Y. Y. Xia, *Chem. Soc. Rev.*, 2016, **45**, 5925.
- 10 J. Kim, M. S. Lee, S. Jeon, M. Kim, S. Kim, K. Kim, F. Bien, S. Y. Hong and J. U. Park, *Adv. Mater.*, 2015, **27**, 3292.
- 11 M. Mohl, A. Dombovari, R. Vajtai, P. M. Ajayan and K. Kordas, *Sci. Rep.*, 2015, **5**, 13710.
- 12 J. H. Park, D. Y. Lee, Y. H. Kim, J. K. Kim, J. H. Lee, J. H. Park, T.-W. Lee and J. H. Cho, *ACS Appl. Mater. Interfaces*, 2014, **6**, 12380.
- 13 M. Vosguerotchian, D. J. Lipomi and Z. Bao, *Adv. Funct. Mater.*, 2012, **22**, 421.
- 14 K. Sun, P. Li, Y. Xia, J. Chang and J. Ouyang, *ACS Appl. Mater. Interfaces*, 2015, **7**, 15314.
- 15 I. N. Kholmanov, S. H. Domingues, H. Chou, X. Wang, C. Tan, J.-Y. Kim, H. Li, R. Piner, A. J. Zarbin and R. S. Ruoff, *ACS Nano*, 2013, **7**, 1811.
- 16 J. H. Chu, D. H. Lee, J. Jo, S. Y. Kim, J. W. Yoo and S. Y. Kwon, *Adv. Funct. Mater.*, 2016, **26**, 7367.
- 17 H.-Z. Geng, K. K. Kim, K. P. So, Y. S. Lee, Y. Chang and Y. H. Lee, *J. Am. Chem. Soc.*, 2007, **129**, 7758.
- 18 G. F. Cai, P. Darmawan, M. Q. Cui, J. X. Wang, J. W. Chen, S. Magdassi and P. S. Lee, *Adv. Energy Mater.*, 2016, **6**, 1501882.
- 19 C. F. Zhang, T. M. Higgins, S.-H. Park, S. E. O'Brien, D. H. Long, J. N. Coleman and V. Nicolosi, *Nano Energy*, 2016, **28**, 495.
- 20 T. Cheng, Y.-Z. Zhang, J.-P. Yi, L. Yang, J.-D. Zhang, W.-Y. Lai and W. Huang, *J. Mater. Chem. A*, 2016, **4**, 13754.
- 21 S. S. Patil, D. P. Dubal, M. S. Tamboli, J. D. Ambekar, S. S. Kolekar, P. G. Romero, B. B. Kale and D. R. Patil, *J. Mater. Chem. A*, 2016, **4**, 7580.
- 22 H. Lin, L. Li, J. Ren, Z. Cai, L. Qiu, Z. Yang and H. Peng, *Sci. Rep.*, 2013, **3**, 1353.
- 23 J. H. Yu, J. F. Wu, H. Z. Wang, A. N. Zhou, C. Q. Huang, H. Bai and L. Li, *ACS Appl. Mater. Interfaces*, 2016, **8**, 4724.

- 24 W. Zhang, Z. X. Yin, A. Chun, J. Y. Yoo, Y. S. Kim and Y. Z. Piao, *ACS Appl. Mater. Interfaces*, 2016, **8**, 1733.
- 25 H. Moon, H. Lee, J. Kwon, Y. D. Suh, D. K. Kim, I. Ha, J. Yeo, S. Hong and S. H. Ko, *Sci. Rep.*, 2017, **7**, 41981.
- 26 H. J. Kim, S. H. Lee, J. Lee, E. S. Lee, J. H. Choi, J. H. Jung and J. Y. Jung, *Small*, 2014, **10**, 3767.
- 27 T. Gao, B. Wang, B. Ding, J.-K. Lee and P. W. Leu, *Nano Lett.*, 2014, **14**, 2105.
- 28 C. F. Guo, T. Sun, Q. Liu, Z. Suo and Z. Ren, *Nat. Commun.*, 2014, **5**, 3121.
- 29 B. Y. Ahn, E. B. Duoss, M. J. Motala, X. Guo, S.-I. Park, Y. Xiong, J. Yoon, R. G. Nuzzo, J. A. Rogers and J. A. Lewis, *Science*, 2009, **323**, 1590.
- 30 H.-J. Choi, S. Choo, P.-H. Jung, J.-H. Shin, Y.-D. Kim and H. Lee, *Nanotechnology*, 2015, **26**, 055305.
- 31 Y. Lee, W.-Y. Jin, K. Y. Cho, J.-W. Kang and J. Kim, *J. Mater. Chem. C*, 2016, **4**, 7577.
- 32 G. A. Salvatore, N. Munzenrieder, T. Kinkeldei, L. Petti, C. Zysset, I. Strebel, L. Buthe and G. Troster, *Nat. Commun.*, 2014, **5**, 2982.
- 33 G. Haacke, *J. Appl. Phys.*, 1976, **47**, 4086.
- 34 H. Wu, D. Kong, Z. Ruan, P. C. Hsu, S. Wang, Z. Yu, T. J. Carney, L. Hu, S. Fan and Y. Cui, *Nat. Nanotechnol.*, 2013, **8**, 421.
- 35 Q. Xu, T. Song, W. Cui, Y. Liu, W. Xu, S.-T. Lee and B. Q. Sun, *ACS Appl. Mater. Interfaces*, 2015, **7**, 3272.
- 36 M. Singh, T. R. Rana, S. Kim, J. H. Yun and J. Kim, *ACS Appl. Mater. Interfaces*, 2016, **8**, 12764.
- 37 S. Bae, H. Kim, Y. Lee, X. Xu, J.-S. Park, Y. Zheng, J. Balakrishnan, T. Lei, H. R. Kim and Y. I. Song, *Nanotechnology*, 2010, **5**, 574.
- 38 W. Xiong, H. Liu, Y. Chen, M. Zheng, Y. Zhao, X. Kong, Y. Wang, X. Zhang, X. Kong and P. Wang, *Adv. Mater.*, 2016, **28**, 7167.
- 39 J. V. D. Groep, P. Spinelli and A. Polman, *Nano Lett.*, 2012, **12**, 3138.
- 40 C. F. Guo and Z. Ren, *Mater. Today*, 2015, **18**, 143.
- 41 M. M. Menamparambath, C. M. Ajmal, K. H. Kim, D. Yang, J. Roh, H. C. Park, C. Kwak, J. Y. Choi and S. Baik, *Sci. Rep.*, 2015, **5**, 16371.
- 42 J. B. In, B. Hsia, J.-H. Yoo, S. Hyun, C. Carraro, R. Maboudian and C. P. Grigoropoulos, *Carbon*, 2015, **83**, 144.
- 43 K. Sheng, Y. Sun, C. Li, W. Yuan and G. Shi, *Sci. Rep.*, 2012, **2**, 247.
- 44 J. Pu, X. H. Wang, R. X. Xu and K. Komvopoulos, *ACS Nano*, 2016, **10**, 9306.
- 45 D. Qi, Z. Liu, Y. Liu, W. R. Leow, B. Zhu, H. Yang, J. Yu, W. Wang, H. Wang, S. Yin and X. Chen, *Adv. Mater.*, 2015, **27**, 5559.
- 46 Z. Niu, L. Zhang, L. Liu, B. Zhu, H. Dong and X. Chen, *Adv. Mater.*, 2013, **25**, 4035.
- 47 V. L. Pushparaj, M. M. Shaijumon, A. Kumar, S. Murugesan, L. Ci, R. Vajtai, R. J. Linhardt, O. Nalamasu and P. M. Ajayan, *Proc. Natl. Acad. Sci. U. S. A.*, 2007, **104**, 13574.
- 48 P. L. Taberna, P. Simon and J. F. Fauvarque, *J. Electrochem. Soc.*, 2003, **150**, A292.
- 49 M. Beidaghi and C. Wang, *Adv. Funct. Mater.*, 2012, **22**, 4501.
- 50 D. Pech, M. Brunet, H. Durou, P. Huang, V. Mochalin, Y. Gogotsi, P.-L. Taverna and P. Simon, *Nat. Nanotechnol.*, 2010, **5**, 651.